Hydrol. Earth Syst. Sci. Discuss., 12, 11739–11782, 2015
www.hydrol-earth-syst-sci-discuss.net/12/11739/2015/
doi:10.5194/hessd-12-11739-2015

Hydrology and Earth System Sciences
Open Access
Discussions

Constraining frequency-magnitude-area relationships for precipitation and flood discharges using radar-derived precipitation estimates: example applications in the Upper and Lower Colorado River Basins, USA

C. A. Orem and J. D. Pelletier

Department of Geosciences, The University of Arizona, 1040 E. 4th Street, Tucson, AZ 85721, USA

Received: 5 October 2015 – Accepted: 14 October 2015 – Published: 10 November 2015

Correspondence to: C. A. Orem (oremc@email.arizona.edu)

Published by Copernicus Publications on behalf of the European Geosciences Union.

Abstract

Flood-envelope curves (FEC) are useful for constraining the upper limit of possible flood discharges within drainage basins in a particular hydroclimatic region. Their usefulness, however, is limited by their lack of a well-defined recurrence interval. In this study we use radar-derived precipitation estimates to develop an alternative to the FEC method, i.e. the frequency-magnitude-area-curve (FMAC) method, that incorporates recurrence intervals. The FMAC method is demonstrated in two well-studied U.S. drainage basins, i.e. the Upper and Lower Colorado River basins (UCRB and LCRB, respectively), using Stage III Next-Generation-Radar (NEXRAD) gridded products and the diffusion-wave flow-routing algorithm. The FMAC method can be applied worldwide using any radar-derived precipitation estimates. In the FMAC method, idealized basins of similar contributing area are grouped together for frequency-magnitude analysis of precipitation intensity. These data are then routed through the idealized drainage basins of different contributing areas, using contributing-area-specific estimates for channel slope and channel width. Our results show that FMACs of precipitation discharge are power-law functions of contributing area with an average exponent of 0.79 ± 0.07 for recurrence intervals from 10 to 500 years. We compare our FMACs to published FECs and find that for wet antecedent-moisture conditions, the 500-year FMAC of flood discharge in the UCRB is on par with the US FEC for contributing areas of $\sim 10^2$ to 10^3 km^2. FMACs of flood discharge for the LCRB exceed the published FEC for the LCRB for contributing areas in the range of $\sim 10^2$ to 10^4 km^2. The FMAC method retains the power of the FEC method for constraining flood hazards in basins that are ungauged or have short flood records, yet it has the added advantage that it includes recurrence interval information necessary for estimating event probabilities.

HESSD
12, 11739–11782, 2015

1 Introduction

1.1 Flood-envelope curves

For nearly a century, the flood-envelope curves (FEC), i.e. a curve drawn slightly above the largest measured flood discharges on a plot of discharge versus contributing area for a given hydroclimatic region (Enzel et al., 1993), have been an important tool for predicting the magnitude of potential future floods, especially in regions with limited stream-gauge data. FECs assume that, within a given hydroclimatic region, maximum flood discharges for one drainage basin are similar to those of other drainage basins of the same area, despite differences in relief, soil characteristics, slope aspect, etc. (Enzel et al., 1993). This assumption enables sparse and/or short-duration flood records over a hydroclimatic region to be aggregated in order to provide more precise constraints on the magnitude of the largest possible (i.e. long-recurrence-interval) floods.

FECs reported in the literature have a broadly similar shape across regions of widely differing climate and topography. For example, FECs for the Colorado River Basin (Enzel et al., 1993), the central Appalachian Mountains (Miller, 1990; Morrison and Smith, 2002), the 17 hydrologic regions within the U.S. defined by Crippen and Bue (1977), the US as a whole (Costa, 1987; Herschy, 2002), and China (Herschy, 2002) are all concave-down when plotted in log-log space, with maximum recorded flood discharges following a power-law function of contributing area for small contributing areas and increasing more slowly at larger contributing areas (i.e. the curve "flattens").

The use of FECs to quantify flood regimes is limited by the lack of recurrence-interval information (Wolman and Costa, 1984; Castellarin et al., 2005) and by the short length, incomplete nature, and sparseness of many flood-discharge records. Without recurrence-interval information, the data provided by FECs are difficult to apply to some research and planning questions related to floods. In the US for example, the 100- and 500-year flood events are the standard event sizes that define flood risk for land planning and engineering applications (FEMA, 2001). FECs also have the potential problem that the maximum flood associated with smaller drainage basins may be biased upward

HESSD
12, 11739–11782, 2015

(or the floods of larger drainage basins biased downward) because there are typically many more records of floods in smaller drainage basins relative to larger drainage basins (because there are necessarily fewer large drainage basins in any hydroclimatic region). That is, the largest flood of record for small drainage basins within a hydroclimatic region likely corresponds to a flood of a larger recurrence interval compared with the largest flood of record for larger drainage basins. In this paper we present a method that includes recurrence-interval information and avoids any sample-size bias that might exist as a function of contributing area.

In this study, a new method for estimating flood discharges associated with user-specified recurrence intervals is introduced that uses radar-derived precipitation estimates, combined with the diffusion-wave flow-routing algorithm, to create frequency-magnitude-area curves (FMACs) of flood discharge. Our method (i.e. the FMAC method) retains the power of the FEC approach in that data from different drainage basins within a hydroclimatic region are aggregated by contributing area, thereby enabling large sample sizes to be obtained within each contributing-area class in order to more accurately constrain the frequencies of past extreme flood events and hence the probabilities of future extreme flood events within each class. The method improves upon the FEC approach in that the complete spatial coverage of radar-derived precipitation estimates provides for large sample sizes of most classes of contributing area (larger contributing areas have fewer samples). The precipitation estimates are then used to predict flood discharges associated with specific recurrence intervals by first accounting for water lost to infiltration and evapotranspiration using runoff coefficients appropriate for different contributing areas and antecedent-moisture conditions, and then routing the available water using a flow-routing algorithm. Predicted flood discharges are presented as FMACs on log-log plots, similar to traditional FECs, except that the method predicts a family of curves, one for each user-defined recurrence interval. These plots are then compared to FECs for the study region (Enzel et al., 1993) and the US (Costa, 1987).

HESSD
12, 11739–11782, 2015

1.2 Study area

This study focuses on the Upper and Lower Colorado River Basins (UCRB and LCRB, respectively; Fig. 1) as example applications of the FMAC method. Although the methods we develop are applied to the UCRB and LCRB in the western US in this study, the methods are applicable to any region of interest where radar-derived precipitation estimates are available (i.e. the entire US and at least 22 countries around the world; Li, 2013; RadarEU, 2014). We focus on the UCRB and LCRB because they have been a focus of flood-hazard assessment studies in the western US and hence the FECs available for them are of especially high quality. In addition, the distinctly different hydroclimatic regions of the UCRB and LCRB (Sankarasubramanian and Vogel, 2003) make working in these regions an excellent opportunity to test and develop the new methods of this study on different precipitation patterns and storm types.

Precipitation and flooding in the LCRB are caused by convective-type storms, including those generated by the North American Monsoon (NAM), and frontal-type and tropical storms sourced from the Pacific Ocean and the Gulf of California (House and Hirschboeck, 1997; Etheredge et al., 2004). In the UCRB, the influence of the NAM and tropical storms is diminished and floods are generally caused by Pacific frontal-type storms (Hidalgo and Dracup, 2003). In both regions, the El Niño Southern Oscillation (ENSO) alters the frequency and intensity of the NAM, tropical storms, and the Pacific frontal systems, and can cause annual variations in precipitation and flooding (House and Hirschboeck, 1997; Hidalgo and Dracup, 2003). Winter storms in both regions are also intensified by the occurrence of atmospheric rivers (Dettinger et al., 2011), which can cause total winter precipitation to increase up to approximately 25 % (Rutz and Steenburgh, 2012). The radar-derived precipitation estimates used in this study record this natural variability in precipitation in the two regions.

The methods used in this study to calculate precipitation and flood discharges of specified recurrence intervals from radar-derived precipitation estimates require a few main assumptions. The first assumption is that of climate stationarity, i.e. the parame-

HESSD
12, 11739–11782, 2015

ters that define the distribution of floods do not change through time (Milly et al., 2008). Climate is changing and these changes pose a challenge to hazard predictions based on the frequencies of past events. Nevertheless, stationarity is a necessary assumption for any probabilistic analysis that uses past data to make future predictions. The results of such analyses provide useful starting points for more comprehensive analyses that include the effects of future climate changes. The second assumption is that the sample time interval is long enough to correctly represent the current hydroclimatic state (and its associated precipitation patterns and flood magnitudes and risks) of the specified study area. Our study uses data for the 1996 to 2004 water years and therefore may be limited by inadequate sampling of some types of rare weather patterns and climate fluctuations within that time interval. To address whether or not the sample time interval used in this study includes major changes in circulation and weather patterns, and therefore is a good representation of climate in the CRB, we investigated the effect of the El Niño Southern Oscillation (ENSO) on precipitation intensity within the UCRB and LCRB. ENSO is a well-known important influence on the hydroclimatology of the western US (Hidalgo and Dracup, 2003; Cañon et al., 2007). In general, winter precipitation in the southwestern US increases during El Niño events and decreases during La Niña events (Hidalgo and Dracup, 2003). The opposite effects are found in the northwestern portions of the US (including the UCRB; Hidalgo and Dracup, 2003). The last assumption of the method is that all basins of similar contributing area respond similarly to input precipitation, i.e. that they have similar flood-generating and flow-routing mechanisms. Specifically, the method assumes that basins of similar contributing area have the same runoff coefficient, flow-routing parameters, basin shape, and channel length, width, and slope. This assumption is necessary in order to aggregate data into discrete contributing-area classes so that the frequency of extreme events can be estimated from relatively short-duration records. In this study, high-recurrence-interval events (i.e. low frequency events) can be considered despite the relatively short length of radar-derived-precipitation-estimate records because the number of samples in the radar-derived record is extremely large, especially for small contributing areas and small

HESSD
12, 11739–11782, 2015

duration floods. For example, for a 1-h time-interval-of-measurement and a contributing area of 4096 km^2 event in the UCRB, there are approximately 40 (number of spatial scale samples) times 55 000 (number of temporal scale samples in nine years of data) samples of precipitation values (and associated modeled discharges obtained via flow routing). As contributing area and time intervals of measurement increase there are successively fewer samples, within any particular hydroclimatic region, thus increasing the uncertainty of the resulting probability assessment for larger areas and longer time periods.

2 Next-Generation-Radar (NEXRAD) data

The specific radar-derived precipitation estimates we use in this study come from the Stage III Next-Generation-Radar (NEXRAD) gridded product, which is provided for the entire US, Guam, and Puerto Rico. NEXRAD was introduced in 1988 with the introduction of the Weather Surveillance Radar 1988 Doppler, or WSR-88D, network (Fulton et al., 1998). The WSR-88D radars use the Precipitation Processing System (PPS), a set of automated algorithms, to produce precipitation intensity estimates from reflectivity data. Reflectivity values are transformed to precipitation intensities through the empirical Z-R power-law relationship,

$$Z = \alpha R^{\beta} \tag{1}$$

where Z is precipitation rate (mm h^{-1}), α and β are derived empirically and can vary depending on location, season, and other conditions (Smith and Krajewski, 1993), and R is reflectivity (mm^6 m^{-3}; Smith and Krajewski, 1993; Fulton et al., 1998; Johnson et al., 1999). Precipitation intensity data are filtered and processed further to create the most complete and correct product (Smith and Krajewski, 1993; Smith et al., 1996; Fulton et al., 1998; Baeck and Smith, 1998). Further information and details about PPS processing are thoroughly described by Fulton et al. (1998).

HESSD
12, 11739–11782, 2015

Stage III NEXRAD gridded products are Stage II precipitation products mapped onto the Hydrologic Rainfall Analysis Project (HRAP) grid (Shedd and Fulton, 1993). Stage II data are hourly precipitation intensity products that incorporate both radar reflectivity and rain-gauge data (Shedd and Fulton, 1993) in an attempt to make the most accurate precipitation estimates possible. The HRAP grid is a polar coordinate grid that covers the conterminous US, with an average grid size is 4 by 4 km, although grid size varies from approximately 3.7 km (north to south) to 4.4 km (east to west) in the southern and northern US, respectively (Fulton et al., 1998).

3 Methods

3.1 NEXRAD data conversion and sampling

NEXRAD Stage III gridded products (hereafter NEXRAD products) for an area covering the Colorado River basin from 1996 to 2005 were downloaded from the NOAA HDSG website (http://dipper.nws.noaa.gov/hdsb/data/nexrad/cbrfc_stageiii.php) for analysis. The data files were converted from archived XMRG files to ASCII format (each data file representing the mean precipitation intensity within each 1 h interval) using the xmrgtoasc.c program provided on the NOAA HDSG website. The ASCII data files were then input into a custom program written in IDL for analysis.

We quantified hourly precipitation intensities ($mm\,h^{-1}$) over square idealized basins (i.e. not real basins, but square basins as shown schematically in Fig. 2) of a range of areas from 16 to 11 664 km^2 (approximately the contributing area of the Bill Williams River, AZ, for readers familiar with the geography of the western US) by successively spatially averaging precipitation-intensity values at HRAP pixel-length scales of powers of two (e.g. 4, 16 $pixel^2$, etc.) and three (e.g. 9, 81 $pixel^2$, etc.; Fig. 2). Spatial averaging is done by both powers of 2 and 3 simply to include more points on the FMACs than would result from using powers of 2 or 3 alone. The number of samples within each contributing area class limited the range of contributing areas used in this study.

HESSD
12, 11739–11782, 2015

UCRB and LCRB boundaries from GIS hydrologic unit layers created by the USGS and provided online through the National Atlas site (http://www.nationalatlas.gov/atlasftp.html#hucs00m) were projected to HRAP coordinates using the methods of Reed and Maidment (2006). These boundaries were used to delineate the region from which precipitation data were sampled from the NEXRAD products, i.e. when averaging precipitation data by powers of two and three a candidate square drainage basin was not included in the analysis if any portion of the square fell outside of the boundaries of the UCRB or LCRB (Fig. 2). Throughout the analysis, the HRAP pixel size was approximated by a constant 4 by 4 km size despite the fact that HRAP pixel sizes vary slightly as a function of latitude (Reed and Maidment, 2006). Our study basins span latitudes between approximately 31 and 43° N resulting in a maximum error of 15 %. However, by keeping the pixel size constant, all pixels could be treated as identical in size and shape allowing us to sample the NEXRAD products in an efficient and automated way over many spatial scales.

For larger contributing areas, necessarily fewer samples are available within a given hydroclimatic region, thus increasing the uncertainty associated with the analysis for those larger contributing-area classes. For the UCRB and LCRB specifically, the uncertainty in the analysis becomes significant for contributing-area classes equal to and larger than $\sim 10^3$ to 10^4 km^2 depending on the recurrence interval being analyzed. Of course, if the hydroclimatic region is defined to be larger, more samples are available for each contributing-area class and hence larger basins can be analyzed with confidence.

In addition to computing precipitation intensities as a function of spatial scale, we averaged precipitation intensities as a function of the time interval of measurement ranging from 1 to 64 h in powers of two by averaging contiguous hourly precipitation intensity records over the entire 9-year study period. This range in time intervals was chosen in order to capture precipitation events that last on the order of ~ 1 h (convective-type storms) to days (frontal-type storms).

HESSD
12, 11739–11782, 2015

3.2 Precipitation and flood calculations

Two types of variables were calculated from the precipitation intensities sampled over the contributing-area and time-interval-of-measurement classes: (1) precipitation discharge, Q_p, and (2) peak flood discharge, Q_{fd}. The variable Q_p is defined as the average precipitation intensity over a basin and time interval of measurement multiplied by the contributing area, resulting in units of $m^3\,s^{-1}$. The variable Q_{fd} is the peak flood discharge ($m^3\,s^{-1}$) calculated via the diffusion-wave flow-routing algorithm for a hypothetical flood triggered by a precipitation discharge, Q_p, input uniformly over the time interval of measurement to idealized square basins associated with each contributing-area class.

The flow-routing algorithm we employ does not explicitly include infiltration and other losses that can further reduce Q_{fd} relative to Q_p. In this study we modeled infiltration and evaporation losses by simply removing a volume of water per unit time equal to one minus the runoff coefficient, i.e. the ratio of runoff to precipitation over a specified time interval, for three antecedent-moisture scenarios. We estimated runoff coefficients for each contributing-area class and each of three antecedent-moisture scenarios using published values for annual runoff coefficients for large basins within the UCRB and LCRB (Rosenburg et al., 2013) and published values for event-based runoff coefficients for small basins modeled with a range of antecedent-moisture conditions by Vivoni et al. (2007) (Fig. 3). On average, estimated runoff coefficients are higher for smaller and/or initially wetter basins. We found the dependence of runoff coefficients on contributing area and antecedent moisture to be similar despite the large difference in time scales between event-based and annual values. Despite the difference in geographic region between our study site and that of Vivoni et al. (2007) (they studied basins in Oklahoma), the runoff coefficients they estimated are likely to be broadly applicable to the LCRB and UCRB given that basin size and antecedent moisture are the primary controls on these values (climate and soil types play a lesser role except for extreme cases).

HESSD
12, 11739–11782, 2015

The flow-routing algorithm routes flow along the main-stem channel of idealized square basins with sizes equal to the contributing area of each contributing-area class. The choice of a square basin is consistent with the square sample areas (see Sect. 3.1) and it allows for basin shape to remain the same (and therefore comparable) over the range of contributing areas used in this study. The main-stem channel, with a length of L (m), was defined as the diagonal distance from one corner to the opposite corner across the square basin (i.e. L is equal to the square root of two times the area of the square basin). This main-stem channel was used in conjunction with a normalized area function to represent the shape of the basin and the routing of runoff through the drainage basin network. By including the normalized area function, we can account for geomorphic dispersion (i.e. the attenuation of the flood peak due to the fact that precipitation that falls on the landscape will take different paths to the outlet and hence reach the outlet at different times) in our analyses. The normalized area function, $A(x)$ (unitless), is defined as the portion of basin area, $A_L(x)$ (m^2), that contributes flow to the main-stem channel within a given range of distances (x) from the outlet, normalized by the total basin area, A_T (m^2; Mesa and Mifflin, 1986; Moussa, 2008). The normalized area function is assumed to be triangular in shape with a maximum value at the mid-point of the main-stem channel from the outlet. The use of a triangular area function is common and such a shape has been shown to approximate the average area function of basins in general (Rodriguez-Iturbe and Valdes, 1979).

A 1-D channel with simplified width and along-channel slope appropriate for channels in the CRB is used to approximate the geometry of the main-stem channel of the idealized basin in the flow-routing algorithm. In addition, values for channel slope, S (m / m), and channel width, w (m), are assigned based on the contributing area of the idealized basin and the results of a least-squares regression to channel-slope and channel-width data from the CRB. We assume here that the assigned channel slopes and widths represent the average value for the entire idealized basin. To find the best approximations for channel slope and width values, we developed formulae that predict average channel slope and channel width as a function of contributing area based on

HESSD
12, 11739–11782, 2015

a least-squares fit of the logarithms of slope, width, and contributing area based on approximately 100 sites in the Colorado River Basin (CRB; Fig. 4). The data used in these least-squares regressions included slope, width, and contributing area information from all sites in the LCRB and southern UCRB presented in Moody et al. (2003) and additional sites from USGS stream-gauge sites from across the CRB.

The assigned channel slope and width values, together with the values of Q_p, were used to calculate the depth-average velocities, V ($m\,s^{-1}$), in hypothetical 1-D main-stem channels of idealized square drainage basins corresponding to each contributing-area and time-interval-of-measurement class. In this study, flow velocity is not modeled over space and time, but rather is set at a constant value appropriate for the peak discharge using an iterative approach that solves for the peak depth-averaged flow velocity, uses that velocity to compute the parameters of the diffusion-wave-routing algorithm, routes the flow, and then computes an updated estimate of peak depth-averaged velocity. To calculate the depth-averaged velocity, V, we used Manning's equation, i.e.

$$V = \frac{1}{n_M} R^{2/3} S^{1/2}, \tag{2}$$

where n_M is Manning's n (assumed to be equal to 0.035), and R is the hydraulic radius (m) calculated with the assigned channel width, and S (m / m) is the assigned channel slope. In order to calculate R, water depth, h, of the peak discharge needed to be determined. In this study h was iteratively solved for based on the peak-flow conditions (i.e. the depth-averaged velocity, V, associated with the peak-flood discharge, Q_{fd}) with h set at 1 m for the first calculation of the flow-routing algorithm. At the end of each calculation, h is recalculated using Manning's equation. These iterations continue until the water depth converges on a value (i.e. the change from the last calculation of h to the next calculation of h is ≤ 0.1 m) corresponding to a specific recurrence interval, contributing-area class, and time-interval-of-measurement class.

The method we used to model flow through the main-stem channel is the diffusion-wave flow-routing algorithm. This approach is based on the linearized Saint-Venant

HESSD
12, 11739–11782, 2015

equations for shallow-water flow in one dimension. To find a simpler, linear solution to Saint-Venant equations, Brutsaert (1973) removed the acceleration term from the equations, leaving the diffusion and advection terms that often provide a reasonable approximation for watershed runoff modeling (Brutsaert, 1973). Leaving the diffusion term in the flow-routing algorithm includes hydrodynamic dispersion of the flood wave in the calculation of the flood hydrograph. In the case where the initial condition is given by a unit impulse function (Dirac function), the cell response function of the channel, q_d (units of s^{-1}), is given by:

$$q_d = \frac{x}{(2\pi)^{1/2} b t_r^{3/2}} \exp\left[-\frac{(x - a t_r)^2}{2b^2 t_r}\right] \quad (3)$$

where x is the distance along the channel from the location where the impulse is input to the channel, t_r is time since the impulse was input into the channel, and the drift velocity a ($m\,s^{-1}$) and diffusion coefficient b^2 ($m^2\,s^{-1}$) are defined as

$$a = (1 + a_0)V(4)b^2 = \frac{V^3}{gSF^2}(1 - a_0^2 F^2) \quad (4)$$

where F is the Froude number, g is the acceleration due to gravity ($m\,s^{-2}$), and a_0 is a constant equal to 2/3 when using Manning's equation (Troch et al., 1994). The large floods modeled in this study are assumed to have critical-flow conditions and therefore the Froude number is set to a constant value of 1.

The unit response discharge, q_{fd} ($m^2\,s^{-1}$), at the outlet of a drainage basin can be computed from Eqs. (3)–(5) by integrating the product of the cell response function $q_d(x,t)$ corresponding to a delta-function input of the normalized area function, $A(x)$, i.e. the spatial distribution of precipitation input. The integral is given by

$$q_{fd}(t_r) = \int_0^{t_p} \frac{Q_p}{w} dt' \int_0^L q_d(x, t_r - t') A(x) dx \quad (5)$$

HESSD
12, 11739–11782, 2015

where t_p is the time interval of measurement over which the unit impulse input (i.e. Q_p) is applied to the idealized square drainage basin, and t_r is the time after the input of the unit impulse that is long enough to capture the waxing the waning portions and the flood peak of the flood wave. The final peak discharge value, or Q_{fd} ($m^3 s^{-1}$), was calculated by multiplying the unit discharge q_{fd} ($m^2 s^{-1}$) by the channel width found through the formula derived from CRB data in Fig. 4, and then selecting the largest value from the resulting hydrograph.

3.3 Recurrence interval calculations

To determine the precipitation-intensity values and Q_p, associated with a user-specified recurrence interval, precipitation intensities for each contributing-area and time-interval-of-measurement class was first ranked from highest to lowest. The relationship between recurrence intervals and rank in the ordered list is given by the probability-of-exceedance equation:

$$\mathrm{RI} = \frac{(n+1)}{m} \tag{6}$$

where RI is the recurrence interval (yr), defined as the inverse of frequency (yr^{-1}) or probability of exceedance, n is the total number of samples in each contributing-area and time-interval-of-measurement scaled to units in years (resulting in units of yr), and m is the rank of the magnitude ordered from largest to smallest (unitless). The resulting precipitation intensities associated with a user-specified recurrence interval and contributing-area and time-interval-of-measurement class was then used to calculate the Q_p value.

At the end of the calculations described above we have datasets of precipitation-intensity, Q_p, and Q_{fd} values for each combination of the eight contributing-area classes, the seven time-interval-of-measurement classes, and the four recurrence intervals. We then find the maximum values of precipitation intensity, Q_p, and Q_{fd} associated with a given contributing-area class and recurrence interval among all values of

HESSD
12, 11739–11782, 2015

the time-interval-of-measurement class (i.e. the values calculated for 1 to 64 h time intervals). This step is necessary in order to find the maximum values for a given contributing area class and recurrence interval independent of the time-interval-of-measurement, i.e. independent of storm durations and associated types of storms. These maximum values are used to plot the FMAC for a given recurrence interval.

3.4 Estimation of uncertainty

Confidence intervals (i.e. uncertainty estimates) were calculated to quantify the uncertainty in calculated precipitation intensities and associated Q_p and Q_{fd} values. In this study we estimated confidence intervals using a non-parametric method similar to that used to calculate quantiles for flow-duration curves (Parzen, 1979; Vogel and Fennessey, 1994). Like quantile calculations, which identify a subset of the ranked data in the vicinity of each data point to estimate expected values and associated uncertainties, we estimated confidence intervals for our predictions based on the difference in Q_p values between each point and the next largest value in the ranked list. This approach quantifies the variation in the precipitation intensity value for a given contributing area and recurrence interval. In some cases the calculated uncertainties for precipitation intensities and associated Q_p and Q_{fd} values are infinite due to the values being past the frequency-magnitude distribution, i.e. there are not enough samples for these values to be determined and there are no finite numbers to sample. These values are not used in this study.

The resulting confidence intervals of precipitation intensity were used to calculate confidence intervals for Q_p and Q_{fd}. Confidence intervals for Q_p values were equal to the confidence intervals for precipitation intensity propagated through the calculation of Q_p (i.e. multiplying by contributing area). Confidence intervals for Q_{fd} values were calculated to be the same proportion of the Q_{fd} value as that set by the precipitation intensity value and it's confidence intervals. For example, if the upper confidence interval was 120 % of a precipitation intensity value, the upper confidence interval for the Q_{fd} value associated with the precipitation intensity value is assumed to be 120 % of the

HESSD
12, 11739–11782, 2015

Q_{fd} value. This approach to propagation of uncertainty treats all other variables in the calculations as constants and additional uncertainty related to regression analyses on variables used in the flow-routing algorithm such as slope, channel width, and runoff coefficients was not included.

3.5 Testing the effects of climate variability

To quantify the robustness of our results with respect to climate variability, we separated the NEXRAD data into El Niño and La Niña months using the multivariate ENSO index (MEI). All months of data with negative MEI values (La Niña conditions) were run together to calculate the precipitation intensity and Q_p values for contributing areas of 16, 256, and 4096 km^2, time intervals of 1 to 64 h, and for 10-, 50-, 100-, and 500-year recurrence intervals. This was repeated with all months of data with positive MEI values (El Niño conditions). Figure 5 shows the distribution of negative and positive MEI values during the 1996 to 2004 water years used in this study.

4 Results

4.1 Channel characteristics and runoff coefficients

Least-squares regression of channel slopes and channel widths from the CRB versus contributing area was used to estimate channel slope, channel width, and runoff coefficients for each idealized basin of a specific contributing-area class. Channel slope decreases as a power-law function of contributing area with an exponent of −0.30 (R^2 = 0.39), whereas channel width increases as a power-law function of contributing area with an exponent of 0.28 (R^2 = 0.65; Fig. 4). These results follow the expected relationships among channel slopes, widths, and contributing area, i.e. as contributing area increases the channel slope decreases and the channel width increases.

HESSD
12, 11739–11782, 2015

Runoff coefficients for wet, medium, and dry antecedent-moisture conditions all decrease with increasing contributing area following a logarithmic function, with the slope of the line decreasing from wet to dry conditions. The fitness of the line to the data also decreases for the wet to dry conditions, with the R^2 values for wet, medium, and dry conditions equal to 0.78, 0.45, and 0.04, respectively. Runoff coefficients decrease with increasing contributing area due to the increased probability of water loses as basin area increases. Also, as expected, runoff coefficients are highest in basins with wet initial conditions that are primed to limit infiltration and evapotranspiration.

4.2 Trends in precipitation intensity

Maximum precipitation intensities (i.e. the maximum among all time-interval-of-measurement classes) for each contributing-area class and recurrence interval decrease systematically as power-law functions of increasing contributing area for all recurrence intervals with an average exponent of -0.22 ± 0.11 (error is the standard deviation of all calculated exponents found from a weighed least-squares regression; average coefficient of determination $R^2 = 0.74$). Note that maximum-precipitation-intensity results are not plotted because they are closely related to the plots of Q_p versus contributing area in Fig. 6, i.e. Q_p is simply the precipitation intensity multiplied by the contributing area. The decrease in maximum precipitation intensity with contributing area can be seen in Table 1, where maximum precipitation intensities over contributing areas of 11 664 km^2 are 65 to 32 % of maximum precipitation intensity values for basin areas of 16 km^2 in both the UCRB and LCRB (Table 1). The largest decrease in maximum precipitation intensity values between the smallest and largest contributing areas were found for the smallest (e.g. 10-year) and largest recurrence interval (e.g. 500-year) for the UCRB and LCRB, respectively. The decrease in maximum precipitation intensity with increasing contributing area suggests that there is a spatial limitation to storms of a given precipitation intensity.

Differences among maximum precipitation intensities for the four recurrence intervals as a function of contributing area are larger in the UCRB than in the LCRB (Table 1).

HESSD
12, 11739–11782, 2015

This larger "spread" in the maximum precipitation intensities in the UCRB relative to the LCRB is also propagated throughout the maximum precipitation and flood discharge calculations. For both the UCRB and LCRB, the difference between the 50- and 100-year recurrence interval values was the smallest (Table 1). These trends show that maximum precipitation intensities vary much more as a function of recurrence interval in the UCRB compared with the LCRB.

Maximum precipitation intensities associated with a 10-year recurrence interval are similar in the LCRB than the UCRB, while intensities were higher in the UCRB than the LCRB for recurrence intervals of 50-, 100-, and 500-years (Table 1). The results of the comparison between the two basins suggest that common (i.e. low-recurrence-interval) precipitation events will have similar maximum precipitation intensities in the UCRB and LCRB, but that rare (i.e. high-recurrence-interval) precipitation events will have higher maximum precipitation intensities in the UCRB than in the LCRB for the same recurrence interval.

4.3 Trends in Q_p

Maximum precipitation discharges (Q_p hereafter) increase with contributing area as power-law functions with an average exponent of 0.79 ± 0.07 (error is the standard deviation of all calculated exponents) based on weighed least-squares regressions on the data ($R^2 = 0.93$) for all recurrence intervals and for both the UCRB and LCRB (Fig. 6). These Q_p values for a given contributing-area class and recurrence interval are the largest values taken from the multiple values calculated for each of the seven time intervals of measurement as explained in Sect. 3.3. By taking the maximum values, the resulting Q_p FMACs approximate the upper envelope of values of a given recurrence interval. In this study the FMAC follows a power-law function that shows that Q_p increases predictably across the range in contributing areas. As with the maximum precipitation intensity results, differences between Q_p values of different recurrence intervals for a given contributing area were larger for the UCRB than the LCRB (Fig. 6).

HESSD
12, 11739–11782, 2015

In general, confidence intervals for Q_p values increase with increasing contributing-area class (Table 1 and Fig. 6). The large values of the highest contributing-area classes and highest recurrence intervals show the spatial limitation of the method, meaning that at these contributing-area classes and recurrence intervals the values are sampled from the largest ranked value and have infinite confidence intervals. These values include the 50-, 100-, and 500-year recurrence intervals for the UCRB and the 100- and 500-year recurrence intervals for the LCRB at the 11 664 km^2 contributing-area class. These values also include the 100- and 500-year recurrence intervals for the UCRB at the 4096 km^2 contributing-area class. Values with infinite confidence intervals are not included in Fig. 6 due to their high uncertainties.

4.4 Trends in Q_{fd}

Maximum Q_{fd} values (hereafter Q_{fd}), i.e. the largest values taken for the multiple values calculated for each time interval of measurement for a given contributing-area class and recurrence interval, were used to plot FMACs for wet, medium, and dry conditions for both the UCRB and LCRB (Fig. 7). In general, FMACs for Q_{fd} values follow the power-law relationship shown in the Q_p FMACs until a contributing area of ≈ 1000 km^2, where the curves begin to slightly flatten or decrease. As with the Q_p values, Q_{fd} values representing some of the higher recurrence intervals converge to the same value (i.e. the value corresponding to the highest precipitation intensity for the contributing-area class) at contributing areas of $\approx 10\,000$ km^2 the and the confidence intervals become infinite (Table 2). This convergence of Q_{fd} values at the largest contributing areas is due to the reduction in the range of values and the number of samples from which to calculate the associated values for each recurrence interval.

In general, The UCRB Q_{fd} FMACs (Fig. 7a, c, and e) are slightly higher in magnitude and span a larger range of magnitudes than the FMACs for the LCRB. For both basins, FMACs for the wet, medium, and dry conditions resulting in the highest, middle, and lowest magnitudes, respectively. This trend is expected due to the lowering of runoff coefficients and available water as conditions become drier.

HESSD
12, 11739–11782, 2015

FMACs of Q_{fd} for the LCRB plot below published FECs for the LCRB and US (Fig. 7b, d, f) at low contributing areas, but exceed the LCRB FEC for contributing areas above ≈ 1000 and $\approx 100\,km^2$ for dry and wet antecedent-moisture conditions, respectively. The FMACs for the LCRB do not exceed the US FEC. All of the FMACs of Q_{fd} for the UCRB exceed the LCRB FEC for wet conditions, with the FMACs of lower recurrence intervals exceeding the curve at higher contributing areas than the FMACs of higher recurrence intervals (Fig. 7a). The 500-year FMAC for wet conditions approximate the US FEC for contributing areas between ≈ 100 to $1000\,km^2$. These results suggests that under certain antecedent-moisture conditions, and in basins of certain contributing areas, the LCRB produces floods that exceed the maximum recorded floods in the LCRB and the UCRB produces floods of magnitudes on par with the maximum recorded floods in the US.

4.5 The effects of ENSO on precipitation

Definitive differences in maximum precipitation intensities and Q_p values were found between months with positive versus months with negative MEI values (Table 3). For very small contributing areas ($16\,km^2$) in the LCRB maximum precipitation intensities and Q_p values are similar during negative and positive MEI conditions. Larger contributing areas (256 and $4096\,km^2$) show higher maximum precipitation intensities during negative MEI conditions regardless of recurrence interval. Values of Q_p show the same trend as the maximum precipitation intensity in the LCRB. In the UCRB, maximum precipitation intensities and Q_p values during negative MEI conditions are higher than those during positive MEI conditions regardless of recurrence interval.

HESSD
12, 11739–11782, 2015

5 Discussion

5.1 Use and accuracy of NEXRAD products

NEXRAD products are widely used as precipitation inputs in rainfall-runoff modeling studies due to the spatially complete nature of the data necessary for hydrologic and atmospheric models (Ogden and Julien, 1994; Giannoni et al., 2003; Kang and Merwade, 2011). In contrast to past studies similar in scope to this study (Castellarin et al., 2005; Castellarin, 2007; Castellarin et al., 2009) we did not use rain-gauge data and only used NEXRAD products to determine the FMACs for precipitation and flood discharges. We favor NEXRAD products due to the spatial completeness of the data.

Intuitively, NEXRAD products that are spatially complete and that average precipitation over a 4 by 4 km area would not be expected to match rain-gauge data within that area precisely (due to the multi-scale variability of rainfall), although some studies have tried to address this discrepancy (Sivapalan and Bloschl, 1998; Johnson et al., 1999). Xie et al. (2006) studied a semi-arid region in central New Mexico and found that hourly NEXRAD products overestimated the mean precipitation relative to rain-gauge data in both monsoon and non-monsoon seasons by upwards of 33 and 55 %, respectively. Overestimation of precipitation has also been noted due to the range and the tilt angle at which radar reflectivity data are collected (Smith et al., 1996). Underestimation of precipitation by NEXRAD products relative to rain gauge data has also been observed (Smith et al., 1996; Johnson et al., 1999), however.

Under- and over-estimation of precipitation by NEXRAD products in relation to rain-gauge data is partly due to the difference in sampling between areal NEXRAD products and point data from rain gauges and partly due to sampling errors inherent to both methods. For example, NEXRAD products include problems such as the use of incorrect Z-R relationships for high intensity storms and different types of precipitation, such as snow and hail (Baeck and Smith, 1998). Also, because of its low reflectivity, snow in the NEXRAD products is measured as if it were light rain (D. Kitzmiller, personal communication, 2012). This means the NEXRAD products likely underestimate snow-

HESSD
12, 11739–11782, 2015

fall and therefore snowfall is not fully accounted for in this study. Rain gauges can also suffer from a number of measurement errors that usually result in an underestimation of rainfall (Burton and Pitt, 2001). In addition, gridded rainfall data derived from rain gauges are not spatially complete and therefore must be interpolated between point measurements to form a spatially complete model of rainfall. It is impossible to discern which product is more correct due to the differences in measurement techniques and errors, but by taking both products and combining them into one, the Stage III NEXRAD precipitation products generate the best precipitation estimate possible for this study. Moreover, it should be noted that 100-year flood magnitude predictions based on regression equations have very large relative error bars (ranging between 37 to 120 % in the western US; Parrett and Johnson, 2003) and that measurements of past extreme floods can have significant errors ranging from 25 to 130 % depending on the method used (Baker, 1987). As such, even a ∼ 50 % bias in NEXRAD-product-derived precipitation estimates is on par or smaller than the uncertainty associated with an analysis of extreme flood events.

5.2 Comparison of the FMAC method to previous studies

Previously published studies have looked at new approaches to approve upon the FEC method. Castellarin et al. (2005) took a probabilistic approach to estimating the exceedance probability of the FEC for synthetic flood data. The authors were able to relate the FECs of certain recurrence intervals to the correlation between sites, the number of flood observations, and the length of each observation. Castellarin (2007) and Castellarin et al. (2009) applied these methods to real flood record data and extreme rainfall events for basins within north-central Italy. Castellarin et al. (2009) also created depth-duration envelope curves of precipitation to relate extreme precipitation events to mean annual precipitation. This group of studies was successful in incorporating recurrence-interval information into the traditional FEC method. However, most of the models presented in these studies were completed with synthetic data or created for design storm processes and require additional analysis and assumptions to be

HESSD
12, 11739–11782, 2015

used on available measured precipitation and flood data. Also, most of the precipitation data used in these past studies was collected using rain gauges (point sources), while only a small subset of data in Castellarin et al. (2009) was sourced from radar-derived precipitation estimates. In contrast to these studies we formulate a simplified method (i.e. the FMAC method) that is readily applicable to any region of interest and can be directly compared to already existing FECs. Also we favor the use of spatially complete radar-derived precipitation estimates in order to apply our methods to ungauged basins.

5.3 Comparison of FMACs to published FECs

FMACs of Q_{fd} exhibit a similar shape and similar overall range in magnitudes as previously published FECs, derived from stream-gauge and paleoflood records, for the LCRB and US (Fig. 7). In general, the FMACs exceed or match published FECs at larger contributing areas, and are lower than or on par with published FECs at the smallest contributing areas (Fig. 7).

All FMACs except the 500-year recurrence-interval curve for the UCRB under wet conditions are positioned well below the US FEC presented by Costa (1987; Fig. 7a). The similarity between the 500-year recurrence interval Q_{fd} FMAC for the UCRB under wet conditions and the US FEC suggests that the US FEC includes floods of larger recurrence-intervals, which are similar in magnitude to the 500-year recurrence-interval floods within the UCRB. The approximation of the US FEC by the 500-year UCRB FMAC is a significant finding due to the fact that the US FEC includes storms from other regions of the US with extreme climatic forcings (i.e. hurricanes, extreme convection storms, etc.).

The Q_{fd} FMACs for the LCRB can be directly compared to the FEC for the LCRB presented by Enzel et al. (1993). At contributing areas smaller than approximately 100 km^2, Q_{fd} FMACs for wet conditions and all recurrence intervals are positioned below the LCRB FEC, but at larger contributing areas Q_{fd} FMACs exceed or approximate the LCRB FEC. Q_{fd} FMACs calculated for medium and dry antecedent conditions show

HESSD
12, 11739–11782, 2015

the same trend, but exceed the LCRB FEC at a larger contributing areas ($\geq 1000\,km^2$). This comparison suggests that although the FMACs overlap the overall range of flood magnitudes of the LCRB FEC, the two methods are not capturing the same trend for extreme flood discharges and the LCRB is capable of producing floods larger than those on record.

The difference in the slope of the FMACs, and specifically the exceedance of the published LCRB FEC, suggests that the two methods are not capturing the same information. This difference may be due to the difference in how the data are sourced for each method. FECs are created as regional estimates of maximum flood discharges and are based on stream-gauging station and paleoflood data. The FECs are then used to provide flood information for the region, including ungauged and unstudied drainage basins. FECs are limited to the number of stream gauges employed by public and private parties and do not include all basins within a region. In general, FECs may underestimate maximum floods in larger basins, relative to smaller basins, because there are a larger number of smaller basins to sample than larger basins. This sample-size problem introduces bias in the record where flood estimates for smaller contributing areas may be more correct than estimates for larger basins. In this study, the regional precipitation information given by the NEXRAD network is used to form the FMAC, therefore taking advantage of the entire region and using precipitation data to calculate flood discharges, rather than directly measuring flood discharges. This sampling scheme allows for much larger sample sizes for the range of contributing areas, therefore minimizing the sample bias of the traditional FEC.

This study aimed to introduce the new method of the FMAC and therefore improve upon the traditional methods of the FEC. By calculating FMACs we provide frequency and magnitude information of possible flood events for a given region in contrast to the FECs that only provide an estimate of the largest flood on record. This information is vital for planning and infrastructure decisions and the accurate representation of precipitation and flooding in design-storm and watershed modeling. In addition, the fact that the FMACs match the FECs for large (500-year) recurrence intervals and do

HESSD
12, 11739–11782, 2015

not exhibit the same trends suggests that the FMACs are capturing different samples than the FECs. This indicates that by using the NEXRAD products, the FMACs may provide a more inclusive flood dataset for a region (especially ungauged areas) than the traditional stream-gauge records.

5.4 Precipitation controls on the form of the FEC

Q_p FMACs were shown to have a strong (average $R^2 = 0.93$) power-law relationship between Q_p and contributing area for all recurrence intervals. Figure 8 shows a conceptualized FEC where the concave-down shape is created when the observed envelope curve diverges from the constant positive power-law relationship between Q_p and contributing area. This diversion creates a "gap" between the two curves and indicates that flood discharge is not a simple power-law function of contributing area. Three mechanisms have been proposed to explain the "gap" and characteristic concave-down shape of FECs: (1) integrated precipitation (i.e. total precipitation over an area) is more limited over larger contributing areas compared to smaller contributing areas (Costa, 1987), (2) a relative decrease in maximum flood discharges in larger contributing areas due to geomorphic dispersion (Rodriguez-Iturbe and Valdes, 1979, Rinaldo et al., 1991, Saco and Kumar, 2004), and (3) a relative decrease in maximum flood discharges in larger basins due to hydrodynamic dispersion (Rinaldo et al., 1991). The first explanation, proposed by Costa (1987), suggests that there is a limitation to the size of a storm and the amount of water that a storm can precipitate. The effect of precipitation limitations may be evidenced by the decreasing maximum precipitation intensities with increasing contributing area. However, the strong power-law relationship between Q_p and contributing area for all recurrence intervals indicates that Q_p is, in general, increasing predictably over the range of contributing areas used in this study. Even if precipitation limitations affect the shape of the curve, this single hypothesis does not account for all of the concave-down shape of each FEC suggesting that other mechanisms are important to creating the characteristic shape. However, it is important to note that the importance of each mechanism may be different for different locations.

HESSD
12, 11739–11782, 2015

5.5 Climate variability in the NEXRAD data

The results from comparing negative and positive MEI conditions in the UCRB and LCRB are generally consistent with ideas about ENSO and how it affects precipitation in the western US. In the LCRB, during negative MEI conditions, small, frequent storms have similar or slightly higher maximum precipitation intensities and Q_p values than during positive MEI conditions. This similarity between the two conditions may be explained by the balancing of increased winter moisture during El Niño in the southwestern US (Hidalgo and Dracup, 2003) and increased summer moisture through the strengthening of the NAM system and the convective storms it produces during La Niña conditions (Castro et al., 2001; Grantz et al., 2007). In general, the strengthening of the NAM may explain the higher maximum precipitation intensities and Q_p values during negative MEI conditions in the LCRB. Strengthening of the NAM may be due in part to the large temperature difference between the cool sea surface of the eastern Pacific Ocean and the hot land surface of the southwestern US and northwestern Mexico during La Niña conditions. The large temperature gradient increases winds inland, bringing the moisture associated with the NAM (Grantz et al., 2007). In the UCRB it is during negative MEI conditions, where the highest maximum precipitation intensities and Q_p values for all recurrence intervals occur. This suggests that the UCRB is affected by ENSO much like the northwestern US, where wetter winters are affiliated with La Niña and not El Niño conditions (Cayan et al., 1999; Hidalgo and Dracup, 2003). It is important to note that this comparison is of intensity rates and not total precipitated moisture so the MEI condition resulting in wetter conditions is not known.

In addition to the ENSO analysis, by investigating previous studies we see that, along with natural yearly precipitation variability, the 1996 to 2004 water years included many atmospheric river events (Dettinger, 2004; Dettinger et al., 2011). It is important that these events were included due to their ability to greatly increase winter precipitation in the UCRB and LCRB (Rutz and Steenburgh, 2012). Atmospheric river events (sometimes known as Pineapple Express events) can also be tied to major Pacific

HESSD
12, 11739–11782, 2015

climate modes such as the ENSO (Dettinger, 2004, 2011), the Pacific Decadal Oscillation (PDO; Dettinger, 2004), and the North Pacific Gyre Oscillation (NPGO; Reheis et al., 2012) in southern California. Unfortunately, correlations between atmospheric river events are unknown and/or less clear for the interior western US. However, all three of these Pacific climate modes shifted during the 9-year study period in ~1998 to 1999 (Reheis et al., 2012) indicating that both positive and negative conditions of the ENSO, PDO, and NPGO exist in the NEXRAD products used in this study.

The presence of distinct trends in maximum precipitation and Q_p values calculated for negative and positive MEI conditions, as well as the information in the literature on atmospheric river events, indicates the NEXRAD products used in this study incorporate circulation-scale weather patterns. In addition, the patterns in maximum precipitation and Q_p values during different MEI conditions agree with common understanding of the effects of ENSO on the western US and provide evidence that the data and methods used in this paper to analyze precipitation are reliable. This analysis shows that the NEXRAD products worked well in this location and that using radar-derived precipitation products may be useful for identifying precipitation and climatic trends in other locations where the FMAC method can be applied.

6 Conclusions

In this study we present the new FMAC method of calculating precipitation and flood discharges of a range of recurrence intervals using radar-derived precipitation estimates combined with a flow-routing algorithm. This method improves on the traditional FEC by assigning recurrence interval information to each value and/or curve. Also, instead of relying on stream-gauge records of discharge, this method uses up-to-date and spatially complete radar-derived precipitation estimates (in this case NEXRAD products) to calculate flood discharges using flow-routing algorithms. This study presents an alternative data source and method for flood-frequency analysis by

HESSD
12, 11739–11782, 2015

calculating extreme (high recurrence interval) event magnitudes from a large sample set of magnitudes made possible by sampling the radar-derived precipitation estimates.

The FMACs for Q_p and Q_{fd} for the UCRB were similar to those produced for the LCRB. In general, all recurrence-interval curves followed the same general trend, indicating that the mechanisms of precipitation and flood discharge are similar for the two basins. However, there were some differences between the two basins. Overall, there were larger differences between curves of different recurrence intervals for the UCRB than the LCRB suggesting a larger range in maximum precipitation intensities, and therefore Q_p and Q_{fd}, in the UCRB relative to the LCRB. For both the UCRB and LCRB the 50- and 100-year recurrence interval curves for all precipitation and discharge FMACs were the most similar. This similarity may mean that although historical discharge records are short, having a 50-year record may not underestimate the 100-year flood as much as one might expect. Also, for Q_p and Q_{fd}, low recurrence-interval values were slightly higher in the LCRB than in the UCRB. This relationship was opposite for high recurrence-interval values. This likely points to a general hydroclimatic difference between the two basins, with the LCRB receiving high intensity storms annually due to the NAM and the UCRB receiving more intense and rarer winter frontal storms.

Power-law relationships between maximum precipitation intensity, Q_p, and contributing area were also found in this study. Maximum precipitation intensities decreased as a power-law function of contributing area with an average exponent of -0.22 ± 0.11 for all recurrence intervals. Q_p values for all recurrence intervals increased as a power-law function of contributing area with an exponent of approximately 0.79 ± 0.07 on average. Based on the constant power-law relationship between Q_p and contributing area, the "gap" or characteristic concave-down shape of published FEC are likely not caused by precipitation limitations.

In general, the FMACs of Q_{fd} calculated in this study are lower than, and exceed, the published FECs for the LCRB at lower and higher contributing areas. All FMACs of Q_{fd} were positioned well below the US FEC except the UCRB 500-year FMAC, which

HESSD
12, 11739–11782, 2015

approximated the US FEC during wet antecedent-moisture conditions. All FMACs of Q_{fd} for all moisture conditions in the LCRB closely approximated the same magnitudes as the published LCRB FEC, but exceeded it for larger contributing areas. The higher estimates of flood discharges at larger contributing areas may be the result of the difference of sampling methods and are likely not erroneous and may be proved true by future events.

Lastly, the approximately 9 years of NEXRAD products were found to be a good representation of climate in the CRB. This conclusion was made based on differences in precipitation between positive and negative ENSO conditions in both the UCRB and LCRB and additional data found in the literature. In general, the UCRB was found to have a hydroclimatic regime much like that of the northwestern US where El Niño conditions result in lower maximum precipitation intensities and amounts and La Niña conditions result in higher maximum precipitation intensities. The LCRB showed a more complex trend with similar maximum precipitation intensities for both El Niño and La Niña conditions.

Here this method is applied to the UCRB and LCRB in the southwestern US, but could be applied to other regions of the US and the world with variable climate and storm types where radar-derived precipitation estimates are available. In addition, this study used set values of contributing area, drainage basin shape, time intervals of measurement, and recurrence intervals that can be changed based on the focus of future studies. Other variables such as snowpack, elevation, and land use should be explored in conjunction with this method to better understand controls on precipitation and flooding.

Acknowledgements. This study was supported by the Jemez River Basin and Santa Catalina Critical Zone Observatory NSF grants EAR-0724958 and EAR-1331408. We would like to thank Vic Baker, Phil Pearthree, Peter Troch, and Katie Hirschboeck for helpful discussions and suggestions.

HESSD
12, 11739–11782, 2015

References

Baeck, M. L. and Smith, J. A.: Rainfall estimates by the WSR-88D for heavy rainfall events, Weather Forecast., 13, 416–436, 1998.

Baker, V. R.: Paleoflood hydrology and extraordinary flood events, J. Hydrol., 96, 77–99, 1987.

Brutsaert, W.: Review of Green's functions for linear open channels, J. Eng. Mech.-ASCE, 99, 1247–1257, 1973.

Burton Jr., G. A. and Pitt, R. E (Eds.): Stormwater effects handbook: a toolbox for watershed managers, scientists, and engineers, Lewis Publishers, Boca Raton, Florida, 2001.

Cañon, J., González, J., and Valdes, J.: Precipitation in the Colorado River Basin and its low frequency associations with PDO and ENSO signals, J. Hydrol., 333, 252–264, 2007.

Castellarin, A.: Probabilistic envelope curves for design flood estimation at ungauged sites, Water Resour. Res., 43, W04406, doi:10.1029/2005WR004384, 2007.

Castellarin, A., Vogel, R. M., and Matalas, N. C.: Probabilistic behavior of a regional envelope curve, Water Resour. Res., 41, W06018, doi:10.1029/2004WR003042, 2005.

Castellarin, A., Merz, R., and Bloschl, G.: Probabilistic envelope curves for extreme rainfall events, J. Hydrol., 378, 263–271, 2009.

Castro, C. L., McKee, T. B., and Pielke Sr., R. A.: The relationship of the North American Monsoon to Tropical and North Pacific surface temperatures as revealed by observational analyses, J. Climate, 14, 4449–4473, 2001.

Cayan, D. R., Redmond, K. T., and Riddle, L. G.: ENSO and hydrologic extremes in the western United States, J. Climate, 12, 2881–2893, 1999.

Costa, J. E.: A comparison of the largest rainfall-runoff floods in the United States with those of the People's Republic of China and the World, J. Hydrol., 96, 101–115, 1987.

Crippen, J. R. and Bue, C. D.: Maximum flood flows in the conterminous United States, U.S. Geological Survey Water Supply Paper 1887, 1977.

Dettinger, M.: Fifty-two years of "Pineapple-Express" storms across the west coast of North America, U.S. Geological Survey, Scripps Institution of Oceanography for the California Energy Commission, PIER Energy-Related Environmental Research, CEC-500-2005-004, 2004.

Dettinger, M. D., Ralph, F. M., Das, T., Neiman, P. J., and Cayan, D. R.: Atmospheric rivers, floods, and the water resources of California, Water, 3, 445–478, 2011.

HESSD
12, 11739–11782, 2015

Enzel, Y., Ely, L. L., House, P. K., Baker, V. R., and Webb, R. H.: Paleoflood evidence for a natural upper bound to flood magnitudes in the Colorado River Basin, Water Resour. Res., 29, 2287–2297, 1993.
Etheredge, D., Gutzler, D. S., and Pazzaglia, F. J.: Geomorphic response to seasonal variations in rainfall in the Southwest United States, Geol. Soc. Am. Bull., 116, 606–618, 2004.
Federal Emergency Management Agency: Modernizing FEMA's flood hazard mapping program: Recommendations for using future-conditions hydrology for the National Flood Insurance Program, Final Report, US Department of Homeland Security, 2001.
Fulton, R. A., Breidenbach, J. P., Seo, D. J., Miller, D. A., and O'Bannon, T.: The WSR-88D algorithm, Weather Forecast., 13, 377–395, 1998.
Giannoni, F., Smith, J. A., Zhang, Y., and Roth, G.: Hydrologic modeling of extreme floods using radar rainfall estimates, Adv. Water Resour., 26, 195–203, 2003.
Grantz, K., Rajagopalan, B., Clark, M., and Zagona, E.: Seasonal shifts in the North American Monsoon, J. Climate, 20, 1923–1935, 2007.
Herschy, R.: The world's maximum observed floods, Flow Meas. Instrum., 13, 231–235, 2002.
Hidalgo, H. G. and Dracup, J. A.: ENSO and PDO Effects on hydroclimatic variations of the Upper Colorado River Basin, J. Hydrometeorol., 4, 5–23, 2003.
House, P. K. and Hirschboeck, K. K.: Hydroclimatological and paleohydrological context of extreme winter flooding in Arizona, 1993, in: Storm-Induced Geologic Hazards: Case Histories from the 1992–1993 Winter in Southern California and Arizona, edited by: Larson, R. A. and Slosson, J. E., Geological Society of America Reviews in Engineering Geology, vol. XI, Boulder, Colorado, 1–24, 1997.
Johnson, D., Smith, M., Koren, V., and Finnerty, B.: Comparing mean areal precipitation estimates from NEXRAD and rain gauge networks, J. Hydrol. Eng., 4, 117–124, 1999.
Kang, K. and Merwade, V.: Development and application of a storage-release based distributed hydrologic model using GIS, J. Hydrol., 403, 1–13, 2011.
Li, B.: Current status of weather radar data exchange, World Meteorological Organization Workshop on Radar Data Exchange, Exeter, UK, April 2013, 2013.
Mesa, O. J. and Mifflin, E. R.: On the relative role of hillslope and network geometry in hydrologic response, in: Scale Problems in Hydrology, edited by: Gupta, V. K., Rodriguez-Iturbe, I., and Wood, E. F., D. Reidel, Dordrecht, Netherlands, 1–17, 1986.
Miller, A. J.: Flood hydrology and geomorphic effectiveness in the central Appalachians, Earth Surf. Process., 15, 119–134, 1990.

HESSD
12, 11739–11782, 2015

Milly, P. C. D., Betancourt, J., Falkenmark, M., Hirsch, R. M., Kundzewicz, Z. W., Lettenmaier, D. P., and Stouffer, R. J.: Stationarity is dead: Whither water management?, Science, 319, 573–574, 2008.
Moody, T., Wirtanen, M., and Yard, S. N.: Regional relationships for bankfull stage in natural channels of the arid southwest, National Channel Design Inc., Flagstaff, AZ, 38 pp., 2003.
Morrison, J. E. and Smith, J. A.: Stochastic modeling of flood peaks using the generalized extreme value distribution, Water Resour. Res., 38, 1305 doi:10.1029/2001WR000502, 2002.
Moussa, R.: What controls the width function shape, and can it be used for channel network comparison and regionalization?, Water Resour. Res., 44, W08456, doi:10.1029/2007WR006118, 2008.
National Atlas: http://www.nationalatlas.gov/atlasftp.html#hucs00m, last access: 8 August 2014.
NOAA HDSG: http://dipper.nws.noaa.gov/hdsb/data/nexrad/cbrfc_stageiii.php, last access: 8 August 2014.
Ogden, F. L. and Julien, P. Y.: Runoff model sensitivity to radar rainfall resolution, J. Hydrol., 158, 1–18, 1994.
Parrett, C. and Johnson, D. R.: Methods for estimating flood frequency in Montana based on data through water year 1998, U.S. Geological Survey Water-Resources Investigations Report 03-4308, 2003.
Parzen, E.: Nonparametric statistical data modeling, J. Am. Statist. Assoc., 74, 105–121, 1979.
RadarEU: http://www.radareu.cz/, last access: 1 August, 2014.
Reed, S. M. and Maidment, D. R.: Coordinate transformations for using NEXRAD data in GIS-based hydrologic modeling, J. Hydrol. Eng., 4, 174–182, 2006.
Reheis, M. C., Bright, J., Lund, S. P., Miller, D. M., Skipp, G., and Fleck, R. J.: A half-million-year record of paleoclimate from the Lake Manix Core, Mojave Desert, California, Palaeogeogr. Palaeocl., 365–366, 11–27, 2012.
Rinaldo, A., Marani, A., and Rigon, R.: Geomorphological dispersion, Water Resour. Res., 27, 513–525, 1991.
Rodriguez-Iturbe, I. and Valdes, J. B.: The geomorphic structure of hydrologic response, Water Resour. Res., 15, 1409–1420, 1979.
Rosenberg, E. A., Clark, E. A., Steinemann, A. C., and Lettenmaier, D. P.: On the contribution of groundwater storage to interannual streamflow anomalies in the Colorado River basin, Hydrol. Earth Syst. Sci., 17, 1475–1491, doi:10.5194/hess-17-1475-2013, 2013.

HESSD
12, 11739–11782, 2015

Rutz, J. J. and Steenburgh, W. J.: Quantifying the role of atmospheric rivers in the interior western United States, Atmos. Sci. Lett., 13, 257–261, doi:10.1002/asl.392, 2012.
Saco, P. M. and Kumar, P.: Kinematic dispersion effects of hillslope velocities, Water Resour. Res., 40, W01301, doi:10.1029/2003WR002024, 2004.
Sankarasubramanian, A. and Vogel, R. M.: Hydroclimatology of the continental United States, Geophys. Res. Lett., 30, 1363, doi:10.1029/2002GL015937, 2003.
Shedd, R. C. and Fulton, R. A.: WSR-88D precipitation processing and its use in National Weather Service hydrologic forecasting, in: Proceedings, Engineering Hydrology: Proceedings of the Symposium Sponsored by the Hydrology Division of American Society of Civil Engineers, 844–848, 1993.
Sivapalan, M. and Bloschl, G.: Transformation of point rainfall to areal rainfall: Intensity-duration-frequency curves, J. Hydrol., 204, 150–167, 1998.
Smith, J. A. and Krajewski, W. F.: A modeling study of rainfall rate-reflectivity relationships, Water Resour. Res., 29, 2505–2514, 1993.
Smith, J. A., Seo, D. J., Baeck, M. L., and Hudlow, M. D.: An intercomparison study of NEXRAD precipitation data, Water Resour. Res., 32, 2035–2045, 1996.
Troch, P. A., Smith, J. A., Wood, E. F., and de Troch, F. P.: Hydrologic controls of large floods in a small basin: central Appalachian case study, J. Hydrol., 156, 285–309, 1994.
Vivoni, E. R., Entekhabi, D., Bras, R. L., and Ivanov, V. Y.: Controls on runoff generation and scale-dependence in a distributed hydrologic model, Hydrol. Earth Syst. Sci., 11, 1683–1701, doi:10.5194/hess-11-1683-2007, 2007.
Vogel, R. M. and Fennesset, N. M., Flow-duration curves I: New interpretation and confidence intervals, J. Water Resour. Bull., 31, 485–504, 1994.
Wolman, M. G. and Costa, J. E.: Envelope curves for extreme flood events, J. Hydraul. Eng.-ASCE, Discussion, 110, 77–78, 1984.
Xie, H., Zhou, X., Hendricks, J. M. H., Vivoni, E. R., Guan, H., Tian, Y. Q., and Small, E. E.: Evaluation of Nexrad Stage III precipitation data over a semiarid region, J. Am. Water Resour. As., 04055, 237–256, 2006.

HESSD
12, 11739–11782, 2015

Table 1. Maximum precipitation intensity and Q_p for the Upper Colorado River Basin (UCRB) and Lower Colorado River Basin (LCRB). Note that data are all sampled from time intervals of measurement ≤ 2 h.

RI	Area (km^2)	Intensity (mm h^{-1})		Q_p (m^3 s^{-1})	
		UCRB	LCRB	UCRB	LCRB
10	16	28.2 ± 0.0	37.5 ± 0.0	125 ± 0	166.6 ± 0
10	64	26.1 ± 0.1	32.5 ± 0.0	464 ± 1	578.0 ± 0
10	144	25.1 ± 0.8	30.0 ± 0.0	1004 ± 31	1198.6 ± 1
10	256	25.0 ± 0.4	27.8 ± 0.1	1774 ± 31	1974.7 ± 4
10	1024	20.7 ± 1.2	19.8 ± 0.1	5887 ± 355	5630 ± 35
10	1296	21.3 ± 1.9	21.7 ± 0.3	7676 ± 681	7820 ± 126
10	4096	15.5 ± 3.0	16.3 ± 0.8	17 682 ± 3462	18 585 ± 890
10	11 664	12.6 ± 4.0	11.0 ± 1.1	40 914 ± 12 864	35 521 ± 3581
50	16	66.6 ± 0.7	56.4 ± 0.0	296 ± 3	250 ± 0
50	64	55.9 ± 1.2	48.0 ± 0.0	993 ± 22	854 ± 1
50	144	55.9 ± 0.9	43.8 ± 0.1	2235 ± 35	1753 ± 5
50	256	55.9 ± 1.4	40.9 ± 0.1	3974 ± 101	2908 ± 6
50	1024	50.8 ± 5.5	33.6 ± 1.4	14449 ± 1569	9560 ± 393
50	1296	50.8 ± 5.8	32.5 ± 2.0	18 287 ± 2091	11 704 ± 707
50	4096	27.6 ± 22.2	30.0 ± 5.2	31 382 ± 25 313	34 126 ± 5969
50	11 664	13.6*	15.4 ± 4.7	68 434*	49 764 ± 15 247
100	16	99.1 ± 0.3	68.6 ± 0.1	440 ± 1	305 ± 0
100	64	100.4 ± 2.5	54.8 ± 0.3	1785 ± 44	974 ± 5
100	144	110.5 ± 1.7	51.9 ± 0.5	4421 ± 70	2075 ± 19
100	256	101.0 ± 2.8	48.4 ± 0.2	7181 ± 201	3440 ± 17
100	1024	68.8 ± 11.0	42.5 ± 2.2	19 578 ± 3139	12 085 ± 630
100	1296	78.5 ± 8.8	43.2 ± 2.1	28 257 ± 3173	15 544 ± 771
100	4096	40.8*	32.0 ± 10.4	46 422*	36 425 ± 11 803
100	11 664	13.6*	20.1*	68 434*	65 011*
500	16	254.0 ± 0.4	81.9 ± 0.7	1129 ± 2	364 ± 3
500	64	229.0 ± 3.1	68.6 ± 1.5	4071 ± 55	1219 ± 26
500	144	219.1 ± 3.2	68.6 ± 3.2	8762 ± 128	2743 ± 128
500	256	219.4 ± 7.3	68.6 ± 3.4	15 600 ± 517	4877 ± 242
500	1024	166.0 ± 44.1	68.6 ± 3.1	47 229 ± 12 554	19 507 ± 884
500	1296	174.6 ± 8.1	65.6 ± 3.4	62 862 ± 2917	23 624 ± 1241
500	4096	81.6 ± 0.0	53.6 ± 53.6*	92 844*	60 930*
500	11 664	13.6*	20.1*	68 434*	65 011*

* Values with infinite confidence intervals, not used in this study.

HESSD
12, 11739–11782, 2015

Table 2. Maximum Q_{fd} for the Upper Colorado River Basin (UCRB) and Lower Colorado River Basin (LCRB). Note that data are all sampled from time intervals of measurement ≤ 2 h.

RI	Area (km^2)	WetQ_{fd} (m^3 s^{-1})		Med Q_{fd} (m^3 s^{-1})		DryQ_{fd} (m^3 s^{-1})	
		UCRB	LCRB	UCRB	LCRB	UCRB	LCRB
10	16	66 ± 1	88 ± 0	37 ± 0	49 ± 0	20 ± 0	27 ± 0
10	64	212 ± 1	263 ± 0	122 ± 0	152 ± 0	71 ± 0	89 ± 0
10	144	417 ± 13	497 ± 1	246 ± 8	293 ± 0	150 ± 5	178 ± 0
10	256	684 ± 12	761 ± 1	412 ± 7	460 ± 1	258 ± 5	288 ± 1
10	1024	1857 ± 112	1775 ± 11	1190 ± 72	1130 ± 7	805 ± 48	776 ± 5
10	1296	2328 ± 207	2373 ± 38	1512 ± 134	1543 ± 25	1038 ± 92	1066 ± 17
10	4096	4335 ± 849	4556 ± 218	3040 ± 595	3191 ± 153	2269 ± 444	2393 ± 115
10	11 664	7847 ± 2467	6812 ± 687	6081 ± 1912	5298 ± 534	4970 ± 1563	4289 ± 432
50	16	156 ± 2	132 ± 0	87 ± 1	73 ± 0	48 ± 1	41 ± 0
50	64	458 ± 10	389 ± 0	264 ± 6	224 ± 0	155 ± 3	132 ± 0
50	144	998 ± 16	727 ± 2	589 ± 9	430 ± 1	358 ± 6	262 ± 1
50	256	1532 ± 39	1121 ± 2	923 ± 23	676 ± 1	578 ± 15	421 ± 1
50	1024	4557 ± 495	3014 ± 124	2919 ± 317	1928 ± 79	1977 ± 215	1308 ± 54
50	1296	5548 ± 634	3551 ± 214	3602 ± 412	2300 ± 139	2474 ± 283	1571 ± 95
50	4096	7694 ± 6206	8368 ± 1464	5389 ± 4347	5850 ± 1023	4024 ± 3246	4343 ± 760
50	11 664	13 145*	9562 ± 2930	10 193*	7317 ± 2242	8326*	6055 ± 1855
100	16	232 ± 1	160 ± 0	129 ± 0	89 ± 0	72 ± 0	50 ± 0
100	64	814 ± 20	444 ± 2	469 ± 11	256 ± 1	275 ± 7	150 ± 1
100	144	1834 ± 29	861 ± 8	1083 ± 17	508 ± 5	659 ± 10	309 ± 3
100	256	2769 ± 78	1327 ± 7	1668 ± 47	798 ± 4	1045 ± 29	499 ± 3
100	1024	6175 ± 990	3812 ± 199	3956 ± 634	2438 ± 127	2677 ± 429	1662 ± 87
100	1296	9329 ± 1048	4715 ± 234	6055 ± 680	3058 ± 152	4160 ± 467	2104 ± 104
100	4096	12 383*	8926 ± 2892	8680*	6294 ± 2039	6471*	4698 ± 1522
100	11 664	13 145*	12 489*	10 193*	9588*	8326*	7821*
500	16	594 ± 1	192 ± 2	331 ± 0	107 ± 1	184 ± 0	59 ± 0
500	64	1856 ± 25	556 ± 12	1069 ± 14	320 ± 7	627 ± 8	188 ± 4
500	144	3634 ± 53	1138 ± 53	2146 ± 31	673 ± 31	1306 ± 19	408 ± 19
500	256	6016 ± 199	1881 ± 94	3624 ± 120	1130 ± 56	2269 ± 75	709 ± 35
500	1024	14 896 ± 3960	6153 ± 279	9544 ± 2537	3945 ± 179	6461 ± 1717	2660 ± 120
500	1296	19 075 ± 885	7170 ± 377	12 379 ± 575	4656 ± 245	8505 ± 395	3198 ± 168
500	4096	22 763*	14 936*	15 947*	10 460*	11 896*	7800*
500	11 664	13 145*	12 489*	10 193*	9588*	8326*	7821*

* Values with infinite confidence intervals, not used in this study.

HESSD
12, 11739–11782, 2015

Table 3. Maximum precipitation intensity and Q_p values for 10, 50, 100, and 500-year recurrence intervals during negative (neg) and positive (pos) Multivariate ENSO Index (MEI) conditions within the Lower Colorado River Basin (LCRB) and Upper Colorado River Basin (UCRB). Note that data are all sampled from time intervals of measurement ≤ 2 h.

Basin	MEI	Area (km^2)	Intensity ($mm\,h^{-1}$)				Q_p ($m^3\,s^{-1}$)			
			10 yr	50 yr	100 yr	500 yr	10 yr	50 yr	100 yr	500 yr
LCRB	neg	16	39	56	69	77	175	250	305	343
	neg	256	31	46	53	69	2206	3251	3741	4877
	neg	4096	21	32	43	54	23 856	36 425	4 8363	60 930
	pos	16	40	64	74	130	179	284	330	576
	pos	256	27	38	47	52	1943	2690	3369	3721
	pos	4096	13	20*	20*	20*	15 229	22 689*	22 689*	22 689*
UCRB	neg	16	41	98	162	254	186	435	721	1129
	neg	256	33	101	155	254	2366	7172	11 012	18 055
	neg	4096	22	34	41	82	25 556	39 013	46 422	92 844
	pos	16	26	51	56	74	115	225	248	330
	pos	256	18	40	51	56	1255	2810	3601	4018
	pos	4096	10	26	27*	27*	10 822	30 034	31 044*	31 044*

* Values with infinite confidence intervals, not used in this study.

HESSD
12, 11739–11782, 2015

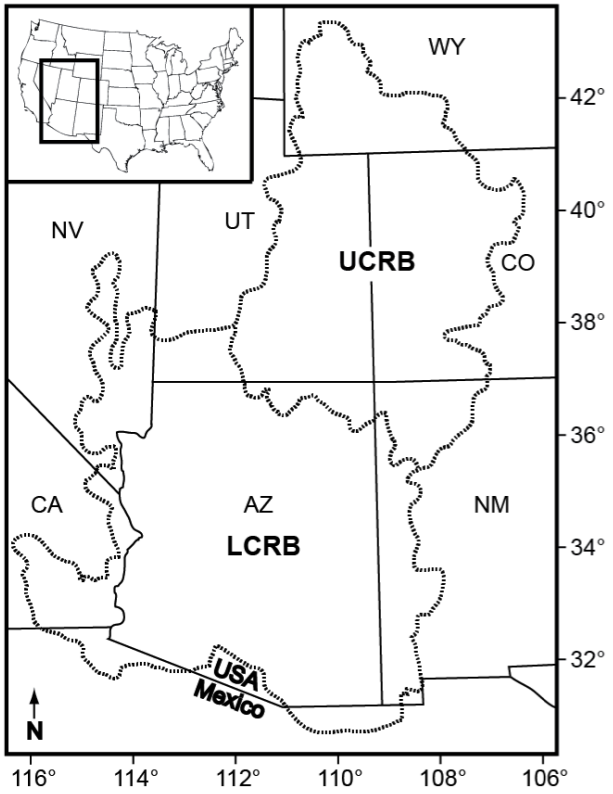

Figure 1. Map showing the locations of the Upper and Lower Colorado River Basins (UCRB and LCRB, respectively) outlined by the dotted line.

HESSD
12, 11739–11782, 2015

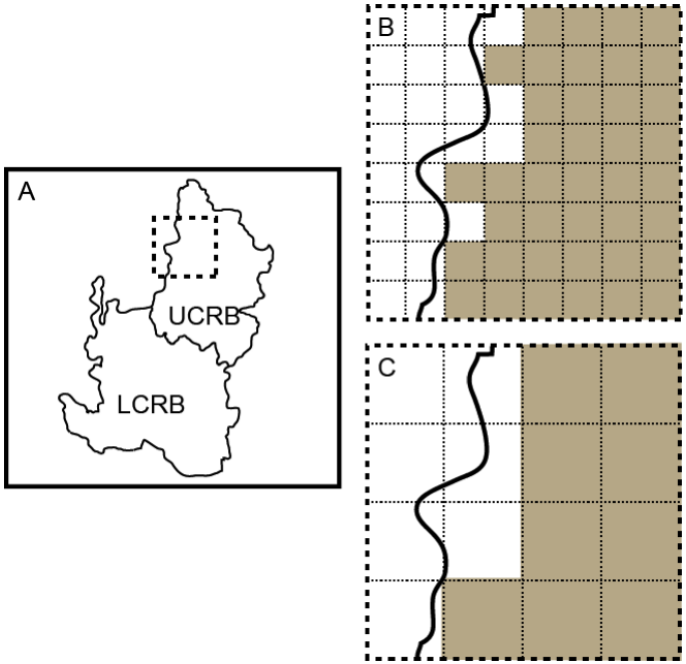

Figure 2. Conceptual diagram of available NEXRAD products for the UCRB and LCRB regions, as well as the sampling scheme used. **(a)** Black-lined box showing the absolute boundary of the available Stage III NEXRAD gridded products and the UCRB and LCRB regions. Area within dashed-line box used to show sampling scheme example **(b, c)**. **(b)** NEXRAD precipitation estimates is sampled in idealized square basins of one size and another size **(c)** as an example (sizes of idealized square basins correspond to powers of 2 and 3, see text). Only idealized-square-basin samples entirely within the region of interest are used (brown boxes) in the analysis.

HESSD
12, 11739–11782, 2015

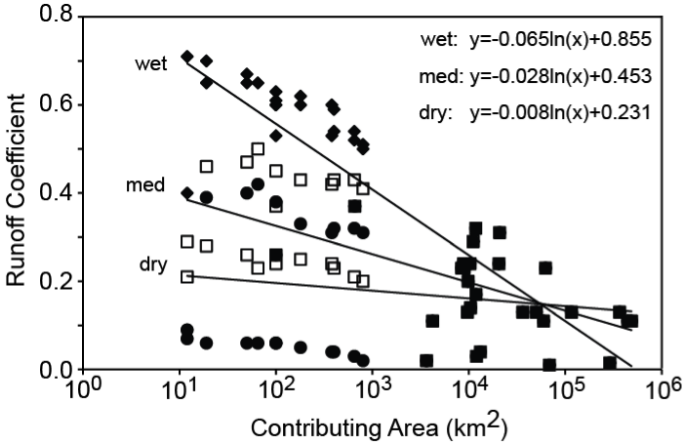

Figure 3. Logarithmic relationships between runoff coefficients and contributing area using modeled data for wet (filled diamonds), medium (open squares), and dry (filled circles) antecedent-moisture conditions (Vivoni et al., 2007) and measured data for larger contributing areas (filled squares; Rosenburg et al., 2013). The medium (open squares) and dry (filled circles) data separate into two distinct groups relating to the precipitation event used to model them, with the lower group and higher group relating to a 12-h, 1-mm h^{-1} event and 1-h, 40-mm h^{-1} event, respectively. All points were used in the least-squares weighed-regression analysis.

HESSD
12, 11739–11782, 2015

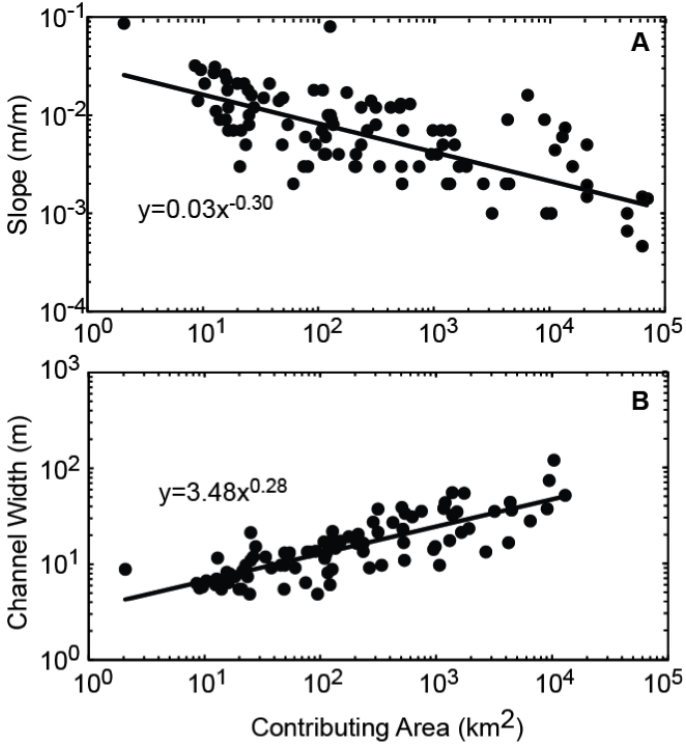

Figure 4. Power-law relationships between channel slope and contributing area **(a)** and channel width and contributing area **(b)** for the Colorado River Basin.

HESSD
12, 11739–11782, 2015

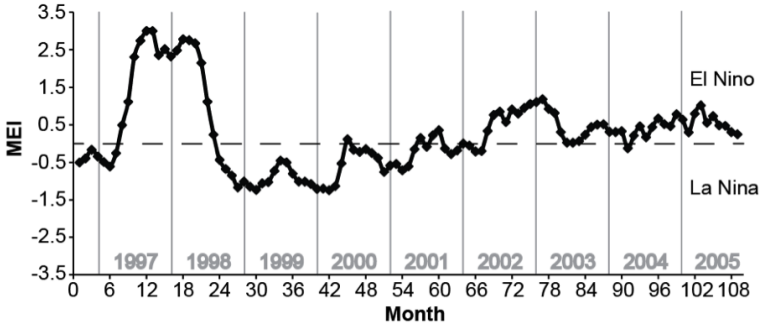

Figure 5. Multivariate ENSO Index (MEI) of months included in Stage III NEXRAD gridded products. Months are numbered from September 1996 to September 2005 with years shown in gray. Dashed black line MEI equal to zero. Positive MEI indicates El Niño conditions, while negative MEI indicates La Niña conditions.

HESSD
12, 11739–11782, 2015

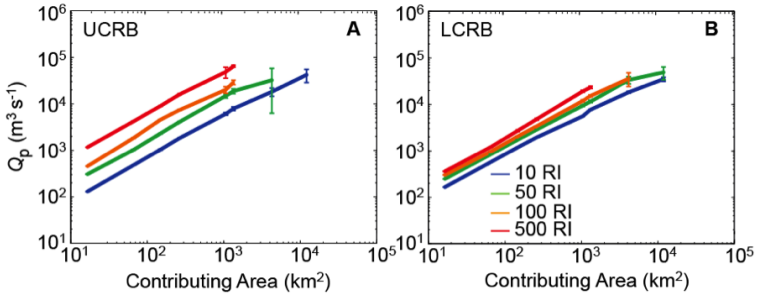

Figure 6. Frequency-magnitude-area (FMA) curves of Q_p versus contributing area for recurrence intervals (RI) of 10, 50, 100, and 500 years for the Upper Colorado River Basin (UCRB; **a**) and the Lower Colorado River Basin (LCRB; **b**).

HESSD
12, 11739–11782, 2015

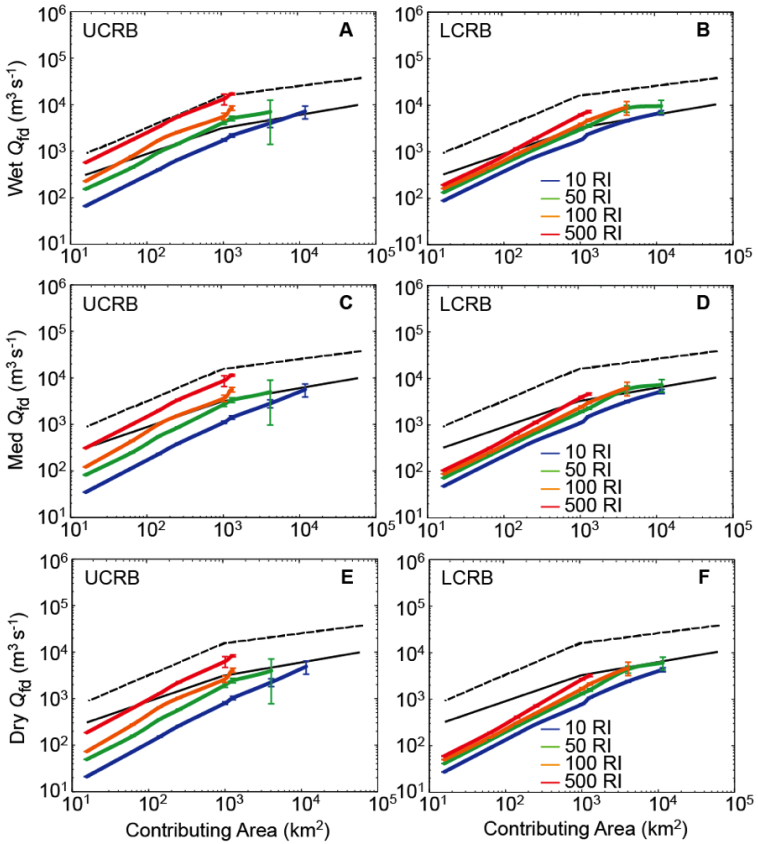

Figure 7. Q_{fd} frequency-magnitude-area curves of 10, 50, 100, and 500 recurrence intervals (RI) and for wet, medium, and dry conditions for the Upper Colorado River Basin (UCRB) and the Lower Colorado River Basin (LCRB). Published FECs (black lines) for the Lower Colorado River Basin (solid black line) from Enzel et al. (1993) and the United States (dashed black line) from Costa (1987) are also shown.

HESSD
12, 11739–11782, 2015

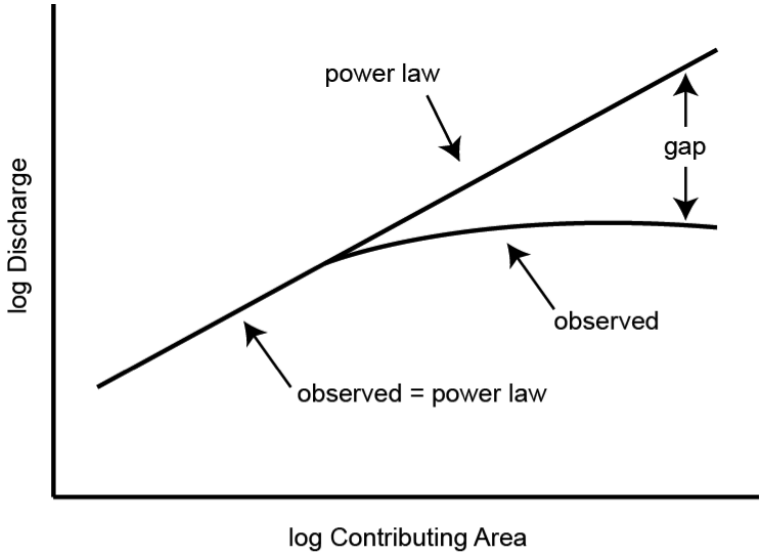

Figure 8. Conceptual diagram of the characteristic concave-down shape of the FEC (observed) shown in comparison to a power-law function between Q_p and contributing area. The "gap" between the observed curve and the predicted power law is caused by precipitation limitations and mechanisms occurring during the routing of water over the landscape.

HESSD
12, 11739–11782, 2015